Check for updates

Received: 4 February 2021 | Revised: 17 June 2021 | Accepted: 7 July 2021

DOI: 10.1002/aic.17371

REACTION ENGINEERING, KINETICS AND CATALYSIS

AIChE JOURNAL

A multi-region and open-source computational fluid dynamic tool for electrochemical systems with three-dimensional electrodes

Alejandro N. Colli | José M. Bisang

Facultad de Ingeniería Química, Universidad Nacional del Litoral, CONICET, Programa de Electroquímica Aplicada e Ingeniería Electroquímica (PRELINE), Santa Fe, Argentina

Correspondence
Alejandro N. Colli, Facultad de Ingeniería Química, Universidad Nacional del Litoral, CONICET, Programa de Electroquímica Aplicada e Ingeniería Electroquímica (PRELINE), Santiago del Estero 2829, S3000AOM Santa Fe, Argentina.
Email: ancolli@gmail.com

Funding information
Universidad Nacional del Litoral; Consejo Nacional de Investigaciones Científicas y Técnicas; Agencia Nacional de Promoción Científica y Tecnológica

Abstract

In this work, a solver, implemented in OpenFOAM, is developed to investigate the mechanisms of ion transport through activated or resistive three-dimensional (3D) electrodes, and also leakage currents in the case of a bipolar connection. The transport model, which accounts for the balance of mass, momentum, species, and electric charge in the fluid, 3D and solid phases, was solved using a multi-region approach. The algorithm permits calculations for a fixed cell potential difference, and also for a current flowing through the cell under galvanostatic control. Analytical models and experimental results of the current and potential distribution are compared with the present tool, obtaining a close agreement between them. The model presented here is supplied as a free source code and can be employed to optimize both cell stack design and system operation conditions.

KEYWORDS
computational fluid dynamics, electrochemical systems, multi-region approach, OpenFOAM, three-dimensional electrodes

1 | INTRODUCTION

An electrochemical reactor is a device in which electrical energy is used to convert raw materials into desired products at the electrodes, anode, and cathode. In contrast, chemical reactions are used to generate electrical energy in a battery or in a fuel cell.[1] Porous, packed, or fluidized beds, also known as three-dimensional (3D) structures, are required as electrodes to increase the space time yield of electrochemical reactors when reactions take place at low current densities like in the case of environmental problems from the process industry;[2] when a high conversion per pass is required such as in metal reduction[3]—metal electrodeposition;[4,5] when there exists a multiple reaction sequence as in the electro-organic synthesis;[6] or when the equilibrium potential for both the main and secondary reactions are close enough like in the negative side of a vanadium redox flow battery.[7] The modeling of these electrochemical systems is necessary for different purposes, including understanding physics, predicting experimental data, optimizing system parameters, or improving cell design.[8]

The operation of electrochemical systems composed of 3D structures involves the simultaneous transport of momentum, species concentration, mass and charge coupled with chemical and electrochemical reactions, and their performance being directly related to these coupled transport phenomena. In a monopolar connection, there is an external electrical contact to each electrode and the cell voltage is applied between every cathode and anode. In this case, anodes and cathodes alternate inside the device and both faces of each central electrode are active, with the same polarity. In this electrical arrangement, theoretical analysis is sometimes restricted to 1D rectangular[9–11] or cylindrical[12,13] designs. First, simplified models helped to compare and decide for a better choice between flow-through and flow-by 3D structures.[14,15] Some theoretical attempts have been made in order to optimize this kind of equipment changing the shape of the electrodes,[16] or predicting the behavior of vertically moving particle bed electrodes.[17] In the case of more complex situations, numerical simulations based on computational fluid dynamic (CFD)

 © 2021 American Institute of Chemical Engineers.

models using commercial software have shown to be the best choice.[18,19]

A bipolar connection requires only two external electrical contacts to each end electrode, one works as a terminal anode and the other as a terminal cathode. The electrodes between the two terminal ones do not have an external electrical connection, and the opposite faces of each of them have different polarities. 3D electrodes can be arranged with a bipolar connection to provide a simpler electrical setup, causing the occurrence of leakage currents that short-circuit each cell in the assembly, producing power loss, corrosion, current inefficiency, and nonuniform current distribution. The magnitude of the leakage current in a stack is a function of the number of cells in it, cell voltage, kinetic parameters, conductivity of the electrolyte, and the geometry of the system. Thus, leakage current is a relevant parameter in the design of bipolar cell stacks.[20,21] The analysis of leakage current proceeds by applying Kirchhoff's laws to an electrical circuit equivalent to the bipolar stack,[20,22–25] by experimental data,[26] or by using more fundamental equations.[27–31]

Some of the drawbacks of the above modeling approaches for electrochemical systems with monopolar or bipolar connections are as follows: (i) for open-access code strategies, they do not allow 2D or 3D modeling, and simplifying assumptions about the geometry, boundary conditions, or kinetics often exclude their application to relevant practical situations. (ii) For commercial software, although 2D modeling and 3D modeling are supported, closed packages may not be flexible for new requirements, the hypotheses behind the "black-box" are doubtful and their license cost can be unaffordable.

Thus, a generalized open-access strategy, based on first principles, is needed in order to contemplate current and potential distributions using any kind of kinetic expressions, properties variation along the spatial coordinates, and operation under potentiostatic or galvanostatic control with monopolar or bipolar connection. Such a proposal would be advantageous to predict real behaviors in pilot or industrial reactors.

Hence, it is the purpose of the present contribution to develop a novel solver, with a new implementation of boundary conditions, in order to analyze the complex coupled transport phenomena in electrochemical systems with 3D electrodes and to assess the accuracy of the numerical tool proposed for these devices. This solver will help to gain a better understanding of the performance for these kinds of systems, providing powerful simulation features in order to analyze a broad range of electrochemical reactors and batteries composed of 3D electrodes and to demonstrate the utility of the CFD-based simulations to aid design considerations.

2 | MATHEMATICAL MODELING

2.1 | Fundamental equations

The 3D electrode is considered as the overlapping of two continua, the solid and fluid phases, for which the following six fundamental equations define the model:

Charge conservation: two Poisson's equations are obtained by combining the current balance with Ohm's law for the fluid (f) and solid (s) phases in the 3D electrode[32]

Calculation subroutine

$$\nabla \cdot (\kappa_{s-f} \nabla \phi_{s-f}) = \pm A_s j. \tag{1}$$

Here, κ, ϕ, A_s, and j are the effective electrical conductivity, the potential, the specific surface area of the 3D structure, and the sum of current densities of all electrochemical reactions occurring at each electrode, respectively. $+A_s j$ is the source term for the solid phase and $-A_s j$ is the source term for the fluid phase in the 3D electrode.

Kinetics for i-th reaction:[33]

$$j^i = \frac{\exp\left(\nu_e^i F/(RT)\eta^i\right) - 1}{\frac{\exp(\alpha^i F/(RT)/\eta^i)}{j_0^i} + \frac{\exp\left(\nu_e^i F/(RT)/\eta^i\right)}{j_{\mathrm{lim,k}}^a} - \frac{1}{j_{\mathrm{lim,k}}^c}}, \tag{2}$$

where j^i and η^i are the current density and the overpotential for each individual electrochemical reaction, respectively, having α^i as apparent charge transfer coefficient, j_0^i as exchange current density, and $j_{\mathrm{lim,k}}^{a\text{-}c}$ is the anodic or cathodic limiting current density of the k-th species. The other symbols in Equation (2) have the usual meaning, that is, ν_e^i is the stoichiometric coefficient for the electron, R is the universal gas constant, T is the temperature, and F is the Faraday constant.

Kinetics at each electrode: assuming that the electrochemical reactions are additive

$$j = \sum_i j^i. \tag{3}$$

Overpotential:

$$\eta^i = \phi_s - \phi_f - E_{\mathrm{rev}}^i. \tag{4}$$

Thermodynamics: given by the Nernst equation

Calculation subroutine

$$E_{\mathrm{rev}}^i = E^{0,i} + \frac{RT}{\nu_e^i F} \ln \prod_k (c_k \gamma_k)^{\nu_k}, \tag{5}$$

where E_{rev}^i, $E^{0,i}$, and ν_k^i are the equilibrium potential, equilibrium potential under standard conditions, and the stoichiometric coefficient for the k-th species entailed in the i-th reaction, respectively. Likewise, c_k and γ_k represent the time-averaged value of concentration and average activity coefficient of the k-th species inside the control volume used in the numerical treatment, respectively.

Time-averaged mass-balance for each k-th species:[34]

Further CFD calculations

$$\boldsymbol{u}\cdot\nabla c_k-\nabla\cdot[(D_k+D_T)\nabla c_k]=R_k^i+A_s\frac{\nu_k^i j^i}{\nu_e^i F\varepsilon}. \tag{6}$$

In Equation (6), the migration term was disregarded assuming the presence of a supporting electrolyte in the fluid phase. However, Equation (6) considers the diffusion and turbulent flows, where D_T and D_k are the turbulent and diffusion coefficients, the latter of the k-th species, respectively. According to Equation (6), the k-th species can participate in several chemical, R_k^i term, or electrochemical reactions, j^i. ε is the void fraction of the 3D structure and $\boldsymbol{u}$ is the time-averaged fluid velocity.

In the calculation method, previously outlined, some variables are highlighted with different colors in order to emphasize the interdependence between equations, requiring an iteration procedure in order to solve the problem.

Therefore, the solver proposed for this mathematical model is valid for any geometrical 3D electrode configuration of an electrochemical reactor; such as porous, packed, fluidized, spouted beds or special arrangements of 3D electrodes made of particles, meshes, expanded metal sheets or foams, felts, and clothes of carbon or metal structures. The above reactors and electrode materials are habitually used in industrial applications.[1]

2.2 | Additional equations

Some parameters in the fundamental equation set require a complementary relationship for their evaluation. Thus, the kinetic calculation of each i-th electrochemical reaction, according to Equation (2), demands an expression for the exchange current density $\left(j_0^i\right)$ and for the limiting current densities ($j_{\mathrm{lim,k}}$) given by[35]

$$j_0^i=\mathrm{cte}^i\prod c_k^{m^i}, \tag{7}$$

and[36]

$$j_{\mathrm{lim,k}}=-\frac{\nu_e^i F k_{\mathrm{m,k}} c_k}{\nu_k^i}, \tag{8}$$

respectively, where the mass-transfer coefficient of the k-th species ($k_{\mathrm{m,k}}$) must be obtained from a dimensionless correlation with Reynolds (Re) and Schmidt (Sc) numbers of the following type[1]

$$k_{\mathrm{m,k}}=a\frac{D_k}{d_e}\mathrm{Re}^b\mathrm{Sc}_k^{1/3}. \tag{9}$$

Here, d_e is the characteristic length of the 3D structure. In Equation (8), ν_k^i is negative for reduced species and positive for oxidized ones, defining the sign of the limiting current density; positive or negative for the anodic or cathodic cases, respectively.

2.3 | Calculation subroutines

The evaluation of other parameters in the fundamental equation set can be performed according to different approaches, also requiring an iterative computation procedure. Therefore, two calculation subroutines are implemented. The first one is related to the evaluation of effective conductivities of the solid and fluid phases ($\kappa_{\text{s-f}}$) in accordance with the Bruggeman equation,[37] which relates the electrical conductivity $\left(\kappa_{\text{s-f}}^0\right)$ to the fluid–solid void fraction

$$\kappa_{\text{s-f}}=\kappa_{\text{s-f}}^0\varepsilon_{\text{s-f}}^{3/2}, \tag{10}$$

assuming in both cases their spatial variation. For example, in the case of gas evolution at the electrodes, the fluid phase is a dispersion of a gas into a liquid and the computation of its conductivity needs the correction of void fraction by the presence of the gas phase.[38,39] This complex issue involves the calculation of the gas fraction taking into account the superficial gas and liquid velocities and also the rise velocity of the bubble swarm, as it was previously detailed.[40] In the case of inhomogeneous or anisotropic solid materials, a specific equation for the effective conductivity is necessary, representing a demanding requirement. The latter subroutine is focused on the calculation of the activity coefficient of each species involved in the electrochemical reactions, which entails a similar procedure to that developed by Kusik and Meissner.[41]

2.4 | Potential distributions

The solution of Equation (1), in order to obtain the potential distribution, is made by means of a multi-region approach,[30] as it is sketched in Figure 1. Thus, separate potential equations for the solid, 3D electrode and fluid regions are solved, because the regions are linked by an interface where the potentials on each region are coupled as detailed in point 2.6 Boundary conditions.

2.5 | Hydrodynamic calculations

The knowledge of the hydrodynamic behavior is necessary in Equation (6) in order to calculate the concentration distribution of each species. For the most general case, the Navier–Stokes equations must be solved under laminar or turbulent flow conditions by means of CFD, which can be performed by using the open-source software OpenFOAM as it was previously reported.[42–44]

In 3D electrodes, $\boldsymbol{u}$ is considered as a time-averaged value taken with respect to a control volume in the medium. Moreover, simulation of porous media is performed by applying velocity and pressure

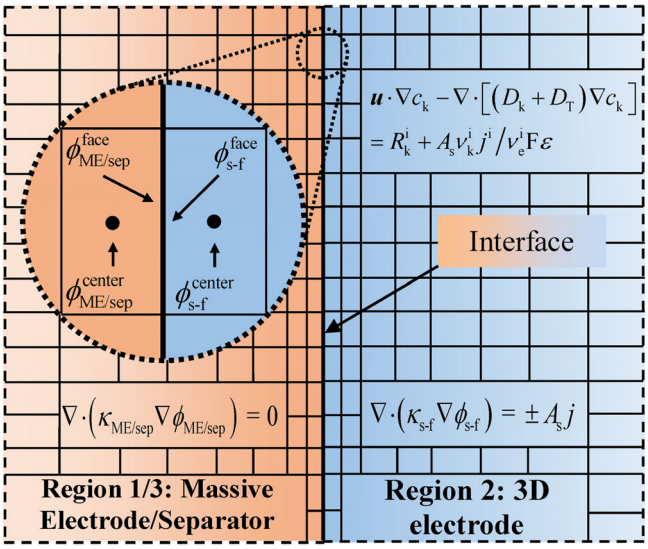

FIGURE 1 Graphical representation of a multi-region approach, showing the discretization near the massive electrode/separator (ME/sep)—Three-dimensional electrode (solid–fluid) interface for a nonuniform structured grid

equations with an additional source term added to the momentum equation as below[45]

$$\nabla \cdot (\boldsymbol{u}) = 0 \tag{11}$$

$$\boldsymbol{u} \cdot \nabla \boldsymbol{u} = -\nabla p + \nabla \cdot \left\{ (\nu + \nu_T) \left[\nabla \boldsymbol{u} + (\nabla \boldsymbol{u})^T \right] \right\} + S. \tag{12}$$

Here ν and ν_T are the kinematic viscosity and the turbulent kinematic viscosity, respectively. The source term (S) can be made up of one or two parts, a viscous loss term and an inertial loss term, creating a pressure drop that is proportional to velocity and velocity squared, respectively, a strategy based on the Darcy–Forchheimer equation[46,47] and implemented in the *porousSimpleFoam* routine already existing in OpenFOAM. Additionally, it is possible to arrive at the same results by adding a porosity momentum source term in all cells or user-specified *cellZone* (a subset of mesh cells) as a source term with the help of the *fvOptions* functionality, which is a collection of run-time selectable finite volume options to manipulate systems of equations by adding sources/sinks, imposing constraints and applying corrections. In this way, it is feasible to solve the steady state for an incompressible fluid under laminar or turbulent flow conditions with implicit/explicit porosity treatment. However, in 3D structures, the velocity profile is often quite uniform and the above hydrodynamic calculations can be simplified.

2.6 | Boundary conditions

For the calculation of the potential distribution in a 3D structure, different types of boundary conditions (BC) can be identified. The trivial case is the insulating container walls, denoted by the subscript w, where

$$\left. \frac{\partial \phi_{s,f}}{\partial n} \right|_w = 0. \tag{13}$$

At the boundary between two electronic conducting regions (ECR), such as the plate acting as current feeder of the 3D structure or the partition wall (PW) in the case of a bipolar electrode, it is valid

$$\phi_s|_{ECR} = \phi_s|_{3D} \tag{14}$$

$$\kappa_s^0 \left. \frac{\partial \phi_s}{\partial n} \right|_{ECR} = \kappa_s \left. \frac{d\phi_s}{dn} \right|_{3D} \tag{15}$$

$$\left. \frac{\partial \phi_f}{\partial n} \right|_{3D} = 0. \tag{16}$$

Likewise, on the edge between the 3D structures with an ionic conducting region (ICR), for example, the electrolyte phase or the separator is

$$\phi_f|_{ICR} = \phi_f|_{3D} \tag{17}$$

$$\kappa_f^0 \left. \frac{\partial \phi_f}{\partial n} \right|_{ICR} = \kappa_f \left. \frac{\partial \phi_f}{\partial n} \right|_{3D} \tag{18}$$

$$\left. \frac{\partial \phi_s}{\partial n} \right|_{3D} = 0. \tag{19}$$

Furthermore, at the connection regions between the electrochemical reactors with power supply, boundary conditions are

$$\phi_s|_{CF}^a = \text{constant} \quad \text{or} \quad \kappa_s^0 \left. \frac{\partial \phi_s}{\partial n} \right|_{CF}^a = \frac{1}{\text{feeder cross-section area}} \tag{20}$$

$$\phi_s|_{CF}^c = 0, \tag{21}$$

where a and c indicate anodic–cathodic sides and CF stands for current feeder; Equations (20) and (21) are applied to both terminal electrodes (TE) for a fixed cell voltage or a galvanostatic operation, respectively. Equations (13–21) are based on Ohm's law in the case of Neumann-type boundary conditions or on potential continuity when a Dirichlet form is used.

It is important to note here that Equations (14–19) state that at the 3D electrode–fluid interface, the current is carried entirely by the pore electrolyte, whereas at the 3D electrode–solid interface, the current is fully drained by the matrix. Likewise, the 3D multi-region approach allows the implementation of the above boundary conditions without the introduction of simplifying

assumptions, often made in previous mathematical modeling studies. For example, a Neumann BC depending on the applied current was used,[9,48–53] or when the potential known a Dirichlet BC was implemented.[3,5,6,11,13–15,17,38,39,54]

Moreover, a Neumann BC for species concentration is accepted at the surface between 3D electrodes and fluid–solids regions, reactor walls, and reactor exit, whereas a Dirichlet type is required at the reactor inlet.

The usual boundary conditions to attend hydrodynamic calculations for a general case were outlined in our previous contributions.[42,44]

3 | IMPLEMENTATION OF THE MODEL

3.1 | Boundary conditions in the multi-region approach

Taking into account Figure 1 for the potential distribution, Equations (14) and (17) can be expressed as follows:

$$\phi_{\text{s-f}}^{\text{face}}\big|_{\text{ECR-ICR}} = \phi_{\text{s-f}}^{\text{face}}\big|_{\text{3D}}. \tag{22}$$

Likewise, Equations (15) and (18) yield

$$\kappa_{\text{s-f}}^{0}\frac{\left(\phi_{\text{s-f}}^{\text{face}} - \phi_{\text{s-f}}^{\text{center}}\right)}{\Delta}\bigg|_{\text{ECR-ICR}} = \kappa_{\text{s-f}}\frac{\left(\phi_{\text{s-f}}^{\text{center}} - \phi_{\text{s-f}}^{\text{face}}\right)}{\Delta}\bigg|_{\text{3D}}. \tag{23}$$

Here, Δ is the distance between the cell center to the interface of each region, and the superscript center denotes the potential in the center of the volume element located immediately next to the interface of each electrode (see Figure 1).

Combining Equation (22) with Equation (23) and solving for $\phi_{\text{s-f}}^{\text{face}}$ results in

$$\phi_{\text{s-f}}^{\text{face}}\big|_{\text{pr}} = \frac{\phi_{\text{s-f}}^{\text{center}}\big|_{\text{pr}}(\kappa_{\text{s-f}}/\Delta)_{\text{pr}} + \phi_{\text{s-f}}^{\text{center}}\big|_{\text{nr}}(\kappa_{\text{s-f}}/\Delta)_{\text{nr}}}{(\kappa_{\text{s-f}}/\Delta)_{\text{pr}} + (\kappa_{\text{s-f}}/\Delta)_{\text{nr}}}, \tag{24}$$

where the subscripts correspond to present region (pr) and next region (nr), and Δ can have a different value in each region. OpenFOAM defines a mixed boundary condition, which allows on each boundary the switching between the fixed value and the fixed gradient situations, given by

$$\phi^{\text{face}} = f\,\text{VR} + (1-f)\left(\phi^{\text{center}} + \text{VGR}\Delta\right). \tag{25}$$

Here, f is the *fractionExpression*, an expression defined by the user. When $f = 1$, Equation (25) gives a Dirichlet boundary condition, and for $f = 0$, it yields a Neumann one. The Robin case, a weighted combination of Dirichlet BC and Neumann BC, is achieved by $0 < f < 1$, where f is calculated as explained below. Comparing Equations (24) and (25) yields

$$\text{VGR} = 0 \tag{26}$$

$$f = \frac{(\kappa_{\text{s-f}}/\Delta)_{\text{nr}}}{(\kappa_{\text{s-f}}/\Delta)_{\text{nr}} + (\kappa_{\text{s-f}}/\Delta)_{\text{pr}}} \tag{27}$$

$$\text{VR} = \phi_{\text{s-f}}^{\text{center}}\big|_{\text{nr}}. \tag{28}$$

Thus, the proposed boundary conditions allow for variations of current and potential along any spatial coordinate.

3.2 | Linearization of the source terms

Nonlinear kinetic expressions, also known as source terms, appearing in Equations (1) and (6), affect not only the potential and concentration distributions within the 3D structure, but also the numerical stability of computations. Then, the sources are linearized by a Taylor series, disregarding higher-order terms, as a function of potential for Equation (1) and of species concentration, Equation (6). The resulting equations are split into two parts, according to

$$j = \sum_{\text{i}}\left[j^{\text{i}} - \phi_{\text{s-f}}\frac{dj^{\text{i}}}{d\phi_{\text{s-f}}}\right]_{\phi_{\text{s-f}}^{0}} + \sum_{\text{i}}\frac{dj^{\text{i}}}{d\phi_{\text{s-f}}}\bigg|_{\phi_{\text{s-f}}^{0}}\phi_{\text{s-f}} \tag{29}$$

$$j^{\text{i}} = \left[j^{\text{i}} - c\frac{dj^{\text{i}}}{dc}\right]_{c_{\text{k}}^{0}} + \frac{dj^{\text{i}}}{dc}\bigg|_{c_{\text{k}}^{0}} c_{\text{k}} \tag{30}$$

$$R_{\text{k}}^{\text{i}} = \left[R_{\text{k}}^{\text{i}} - c\frac{dR_{\text{k}}^{\text{i}}}{dc}\right]_{c_{\text{k}}^{0}} + \frac{dR_{\text{k}}^{\text{i}}}{dc}\bigg|_{c_{\text{k}}^{0}} c_{\text{k}}, \tag{31}$$

where the first term was treated explicitly and the second part was treated implicitly. It is always important to ensure the implicit treatment is used only when it results in a negative slope of the linearized term. Thus, when the slope of the linearized source terms can assume positive and negative values (cathodic or anodic currents), in different regions of the domain, negative contributions should be treated as implicit and positive contributions as explicit. For that purpose, OpenFOAM provides a special source term function, SuSp in which the implicit/explicit treatment is automatically performed.[55] In order to improve stability, even more by slowing down the change in the value of the potential or concentration from iteration to iteration, an implicit under-relaxation method is applied.[56] The source terms in Equations (1) and (6) are implemented via a user-specified finite volume option given by the shorthand *fvOptions*, allowing it to be manipulated at run time without the need of programming.

3.3 | Source code and tutorial

The present strategy, a coupling of Equations (1–10) and BC (13–21) by the FVM using OpenFOAM, is supplied as a GitHub link[57] so that the

reader makes use of it. In addition, with the aim of achieving a better understanding, a flowchart of the algorithm is shown in Figure 2. Thus, a new solver, a new BC, which allows for the calculation of current and potential distributions in 3D electrodes, fluid and solid regions using the multi-region approach, is provided. The solver for the solution of the mathematical model requires a mesh (geometry) definition of each 3D electrode–solid–fluid region in *Constant/regionProperties*. Thermodynamic, physicochemical, and kinetic parameters are fed before its running and are stored in a file called *transporProperties*, located inside the folder *Constant*. Finally, a concise example and a tutorial on how to use the validated tool are provided, which have been tested in OpenFOAM 7.[58]

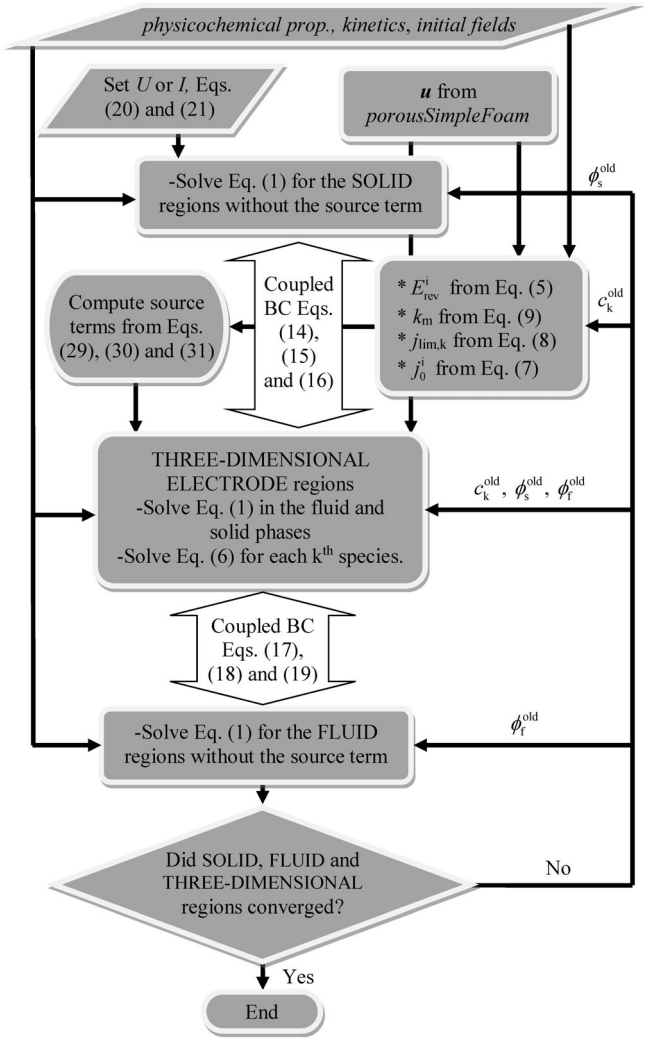

FIGURE 2 Flowchart for solving the proposed current-potential distribution algorithm for a monopolar or bipolar electrochemical reactor composed of three-dimensional electrodes under a fixed cell potential difference or galvanostatic control by the multi-region approach

4 | RESULTS AND DISCUSSION

4.1 | Computational aspects

Table 1 reports on resolution parameters, algorithm control, and numerical schemes imposed for the computation of each field used in the present strategy. It must be pointed out that the numerical settings allowed to satisfactorily predict all the situations simulated so far. However, for situations outside those tested here, a user may need a different numerical setting for which OpenFOAM provides an extensive set of options.

4.2 | Verification and validation of the solver by comparison with previous studies

4.2.1 | Current and potential distribution in plane porous electrodes

Considering a 1D mathematical model for a porous electrode as depicted in Figure 3A and a Tafel kinetics, which is obtained from Equation (2) assuming that $j_{\mathrm{lim,c}}$, $j_{\mathrm{lim,a}}$, and $b_{\mathrm{a\text{-}c}}$ tend to infinity, Newman et al.[9,50] found that the dimensionless reaction rate (jA_sV/I) as a function of the dimensionless distance (x/L) is given by

$$J = \left(2\theta^2/\delta\right)\sec^2(\theta X - \sigma), \tag{32}$$

TABLE 1 Numerical settings used in the present strategy

Resolution control (fvSolution)						
Field	**Solver**	**Preconditioner**	**Tolerance**	**relTol**	**Convergence**	**Relaxation factor**
$\phi_{\mathrm{s\text{-}f}}$	PCG	DIG	1×10^{-10}	0	1×10^{-5}	0.99
c_k	PBiCG	DILU	1×10^{-7}	0	1×10^{-5}	—

Numerical schemes (fvSchemes)					
Field	**gradSchemes**	**divSchemes**	**laplacianSchemes**	**interpolationSchemes**	**snGradSchemes**
$\phi_{\mathrm{s\text{-}f}}$	leastSquares	—	Gauss linear corrected	Linear	Corrected
c_k	leastSquares	Gauss linear	Gauss linear corrected	Linear	Corrected

where

$$\tan\theta = 2\delta\theta/\left[4\theta^2 - \tau(\delta-\tau)\right],\ \tan\sigma = \tau/(2\theta),\ 0<\theta<\pi, \tag{33}$$

and

$$\delta = \frac{\tau(\kappa_s+\kappa_f)}{\kappa_s},\quad \tau = \frac{L^2|I|}{b_{a\text{-}c}\kappa_f V}. \tag{34}$$

This model represents a case where reactants are present at high concentration, both electrodes are short in the axial direction, and high flow rates are employed in order to avoid concentration variations. Figure 3B depicts the comparison between the present multi-region tool and Equation (32), for J, or numerical calculations from Newman and Tiedemann,[50] for $\phi_{s\text{-}f}$, where no analytical equation exists. A perfect match between them can be observed. From Equations (32–34), it can be seen that the dimensionless reaction rate (J) is independent of j_0A_s. The same conclusion is obtained using different j_0 and A_s values with the proposed tool. However, from the numerical procedure, it can be stated that both potentials of the solid and fluid phases are dependent on j_0A_s.

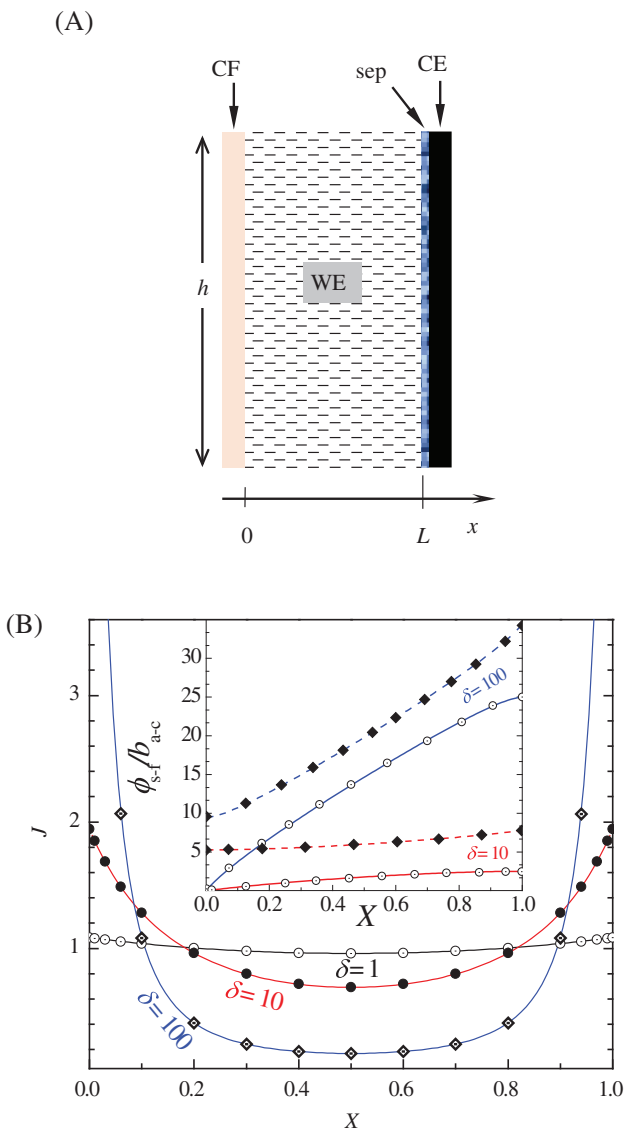

FIGURE 3 (A) Schematic view of a three-dimensional structure. CE, counter electrode; WE, three-dimensional working electrode; CF, current feeder; sep, separator. (B) Dimensionless current distribution for Tafel polarization $\tau = 0.5\delta$. Inset: Dimensionless potential distribution. Full lines: solid phase. Dashed lines: fluid phase. $j_0A_s = 40$ A m^{-3}; $\kappa_s = \kappa_f = 10$ S m^{-1}; $b_{a\text{-}c} = 0.05$ V. $L = 0.025$ m

4.2.2 | Porous electrodes with varying electrolyte conductivity

Guo et al.[59] reported that ionic conductivity in the air cathode of a polymer electrolyte membrane (PEM) fuel cell changes with position inside the active layer depending on the ionomer loading. The conductivity profile of the solid or fluid phases has a strong influence on the air cathode performance, where its modeling is a challenging task. The cathode region of a PEM fuel cell was modeled by Diwakar and Subramanian[51] for a 1D geometry, which is again depicted by Figure 3A. In order to obtain an analytical solution, the above authors considered that the solid-phase potential is zero, a linear kinetics is valid, concentration gradients are absent, the process is assumed to be at a steady state, and a variation of the conductivity according to

$$\kappa_f = \kappa_{av} 2X, \tag{35}$$

where κ_{av} is the average value of the effective conductivity inside the active layer with a thickness L. Thus, the following expression for the dimensionless electrolyte current density (J_f) was obtained

$$J_f(X) = \frac{\sqrt{X}\,\mathrm{Real}\left[\mathrm{BesselJ}\left(1,-2\xi\sqrt{-X/2}\right)\right]}{\mathrm{Real}\left[\mathrm{BesselJ}\left(1,-2\xi\sqrt{-1/2}\right)\right]}, \tag{36}$$

where BesselJ is the Bessel function of the first kind, and ξ is the dimensionless exchange current density, according to[51]

$$\xi = \sqrt{\frac{A_s j_0 F L^2}{RT\kappa_{av}}}. \tag{37}$$

Finally, the dimensionless electrolyte potential (χ) was obtained from Equation (36) according to

$$\chi = dJ_f/dX, \tag{38}$$

where

$$J_f = \frac{j_f}{j_{app}},\ \chi = \frac{A_s j_0 F L}{RT\, j(L)}\phi, \tag{39}$$

where $j(L)$ is the current density evaluated at $x = L$, j_f is the electrolyte (fluid) current density, and j_{app} is the applied current density at the current feeder.

In order to compare the analytical expression, Equation (36), with the proposed numerical procedure, the conductivity of the solid matrix was chosen as 1×10^6 S m^{-1}, while the conductivities of the current feeder, anode, and electrolyte between the anode and the porous structure are unimportant. For numerical calculations, $L = 0.025$ m, $A_s = 1000$ m^{-1}, $T = 298$ K, and $j_0 = 4.11 \times 10^{-2}$, 6.57×10^{-1}, 2.63 A m^{-2} in order to have $\xi = 1$, 4, and 8 were chosen, respectively.

Figure 4 depicts the dimensionless electrolyte potential as a function of dimensionless distance (X). The dimensionless electrolyte current density vs X for different dimensionless exchange current densities is shown in the inset. It is seen that the numerical approach (points) reproduces the analytical one (solid lines), and when ξ increases, the dimensionless variables become less uniform. Moreover, the numerical treatment allows much more complex situations to be solved, that is, with different functionalities for the conductivities of the fluid and solid phases, 3D geometries with potential and current varying in spatial directions, concentrations of k species with any kind of kinetic control and diverse hydrodynamic situations inside the porous region.

4.2.3 | Mesh cylindrical electrode with inner or outer counter electrode

Figure 5 schematically shows an axisymmetric view of a cylindrical electrochemical reactor with a mesh working electrode. Part (A) corresponds to the configuration with the outer counter electrode and Part (B) to the inner case. These cases were analyzed by Kreysa et al.[12] and Colli and Bisang[36] assuming that: (i) the void fraction and the surface area per unit electrode volume are uniform, (ii) the electrolyte velocity is constant across the cross-section of the reactor, and (iii) a single electrode reaction takes place under limiting current conditions without a concentration change between the inlet and outlet of the reactor. Therefore, the dimensionless potential distribution inside the 3D electrode is given by

$$\frac{[E(r)-E(r_i)]\kappa_f}{j_{lim}A_s} = \frac{1}{2}\left(\frac{r^2-r_i^2}{2} - r_{ref}^2 \ln\frac{r}{r_i}\right), \tag{40}$$

where $r_{ref} = r_i$ for the outer counter electrode case and $r_{ref} = r_e$ when the counter electrode is internal, and

$$E(r) = \phi_s - \phi_f(r). \tag{41}$$

The comparison between analytical (solid lines) and numerical (points) results is reported in Figure 5C, showing an excellent

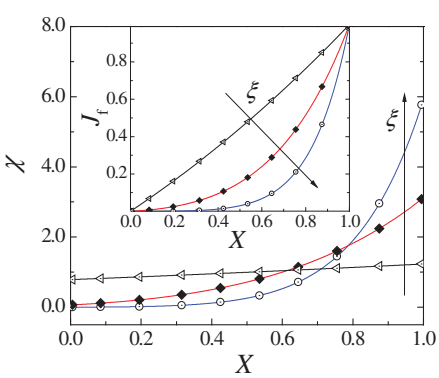

FIGURE 4 Dimensionless electrolyte potential as a function of the dimensionless distance for different values of ξ given by Equation (37) (1, 4, 8). Inset: Dimensionless electrolyte current density as a function of the dimensionless distance. Solid lines: analytical expression according to Equation (36).[51] Points: numerical solution according to the present approach

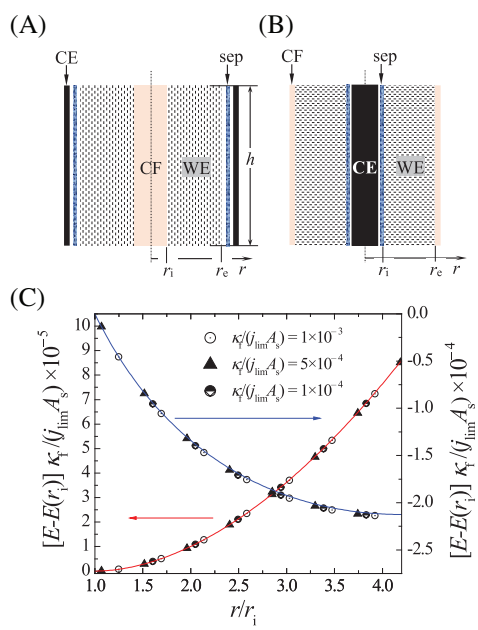

FIGURE 5 Schematic axisymmetric view of the two arrangements of cylindrical electrochemical mesh working electrodes used in the mathematical model. (A) Outer counter electrode. (B) Inner counter electrode. CE, counter electrode; WE, three-dimensional (mesh) working electrode; CF, current feeder; sep, separator. (C) Distribution of the electrode potential as a function of the radial position, r. Outer counter electrode arrangement in right ordinate. Inner counter electrode arrangement in left ordinate. r_i is the internal radius of the mesh electrode. Full lines: theoretical behavior according to Equation (40). Symbols: Numerical results for different κ_f/jA_s. $r_i = 5$ mm, $r_e = 21$ mm. $\kappa_s = 1 \times 10^7$ S m^{-1}. $\kappa_f = 10$ S m^{-1}. $A_s = 1000$ m^{-1}. $j_{lim} = -10, -50, -100$ A m^{-2}

agreement between both data sets, which corroborates that the solver is appropriate for these calculations.

4.2.4 | Bipolar 3D electrode

Taking into account a 1D bipolar mesh electrode, as depicted in Figure 6A, imposing a reversible mass-transfer controlled reaction at low overpotentials, that is,

$$j = j_{\text{lim}}[1 - \exp(\eta/b)] \simeq |j_{\text{lim}}|\eta(X)/b, \tag{42}$$

the following analytical expression was deduced[48]

$$\eta(X) = \eta(0)\frac{\sinh[\Omega L(1/2 - X)]}{\sinh[\Omega L/2]}, \tag{43}$$

where

$$\eta(0) = \frac{IL\tanh[\Omega L/2]}{\Omega V \kappa_f}, \quad \Omega^2 = \frac{A_s|j_{\text{lim}}|}{\kappa_f b}, \tag{44}$$

and the by-passed fraction of the total current is

$$I^*/I = \text{sech}[\Omega L/2]. \tag{45}$$

Figure 6B shows the comparison between the present numerical calculation (full lines) and analytical results (points), for half of the bipolar 3D electrode. A perfect match among them can be observed in the case of high solid-phase conductivity while others ratios between conductivities are also shown. It is observed that a decrease in the conductivity of the solid phase reduces the volumetric current, the overpotential, and increases the by-passed fraction.

Figure 7 displays numerical results of concentration, current density, and overpotential distributions along the electrode thickness (x coordinate) for different axial positions (y = 2, 50 and 98 mm) for a bipolar 3D electrode 100 mm long. For comparison, the full black circles in the inset correspond to results from a simplified numerical 1D model that neglects concentration changes.[48] Table 2 summarizes the results of experiments performed at different total currents[48] and numerical calculations in accordance with the present approach where

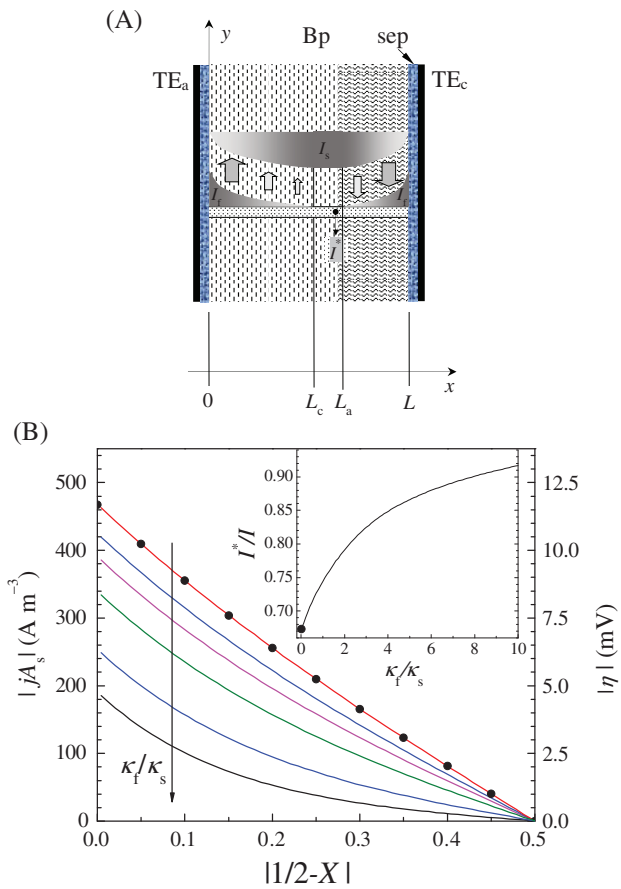

FIGURE 6 (A) Diagram of an electrochemical stack with one bipolar three-dimensional electrode. Schematic representation of the current variations in the solid and fluid phases. $TE_{a\text{-}c}$: terminal anode/cathode, Bp: bipolar three-dimensional electrode. (B) Current and overpotential distributions for a mass-transfer controlled reaction at low overpotential. $\kappa_f/\kappa_s = 1 \times 10^{-4}$, 0.5, 1, 2, 5, and 10. Inset: by-passed fraction of the total current as a function of the ratio of conductivity of the fluid and solid phases. Full lines: numerically obtained results. Black points: analytical results. $j_{\text{lim}} = 2$ A m^{-2}; $\kappa_f = 10$ S m^{-1}; $b = 0.05$ V; $L = 0.03$ m; $A_s = 1000$ m^{-1}

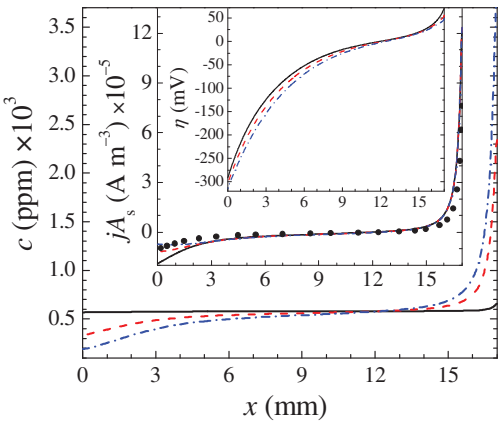

FIGURE 7 Concentration, current density, and overpotential distributions inside a bipolar packed bed electrode 100 mm long (y coordinate), as a function of the thickness (x coordinate). $I = 2.5$ A. $c_{\text{in}} = 580$ ppm, $A_s = 6420$ m^{-1}. Full black lines: $y = 2$ mm. Dashed red lines: $y = 50$ mm. Dot-dashed blue lines: $y = 98$ mm. Full black circles: simplified numerical results from González Pérez and Bisang[48]

a close agreement can be observed between the computed and measured values of the thickness of the cathodic part at the bipolar 3D electrode, L_c (See Figure 6A). Likewise, the theoretical by-passed fraction of the total current agrees well with the estimated values from experimental results. Finally, it must be pointed out that the numerical 3D model with species concentration variations allows the user to inspect different regions of the electrode in order to inquire about side reactions or underused electrode zones.

A mesh bipolar electrode with irreversible reactions was also analyzed with the present tool and compared with previously reported experimental results.[49] In order to numerically simulate the irreversible system, a Heaviside function was used, that is, multiplying Equations (29) and (30) by a function that is 1 when the overpotential is positive and 0 when it is negative for the anodic reaction and the opposite for the cathodic reaction, with the aim of disregarding oxygen reduction and anodic copper dissolution. Table 3 depicts experimental results[49] and theoretical data obtained with the present model at $y = 50$ mm for both cathodic thickness and by-passed current, where an excellent agreement between both data sets can be observed. Moreover, the proposed numerical strategy allows the spatial variation of L_c to be predicted in the previous two cases.

4.3 | Stack of bipolar electrodes

Finally, the modeling strategy proposed in this article was tested with a bipolar stack composed of two TE, 9 bipolar electrodes (Bp), and 10 separators (sep) between them, as sketched in Figure 8A. For symmetry reasons, only the upper half of the cell was considered for numerical calculations.

Based on the solid-phase conductivity of the electrodes, three cases were analyzed here: (i) planar electrodes with infinite conductivity, called Model 1; (ii) planar electrodes with finite conductivity in the partition wall of bipolar electrodes, Model 2; and (iii) a 3D structure with a resistive solid phase, Model 3.

TABLE 2 Comparison between the numerical simulation and experimental results from González Pérez and Bisang[48]

I (A)	c_{in} (ppm)	$L_{c,exp}$ (mm)	$L_{c,th}$ (mm)	I^*/I_{exp} (%)	I^*/I_{th} (%)
2	617	12	**11.98**	5.89	**6.54**
2.5	580	12	**12.18**	3.81	**6.82**
3	588	12	**12.46**	8.29	**6.62**

Bold values indicate present result.

Figure 8B shows the fraction of the total current drained for each electrode as a function of its position along the reactor and in accordance with the physicochemical and kinetic parameters reported in Table 4. Table 5 summarizes the main results. The red line in Figure 8B corresponds to Model 1 and it reproduces the behavior reported by Colli and Girault.[29] The black line represents Model 2, which agrees with the results according to the proposal by Colli and Bisang.[30] The blue line was calculated with Model 3. The dashed lines represent analytical results based on an electrical analog to calculate the current distribution along the reactor according to Burnett and Danly,[20] Equation (46), by using a cell potential difference for the stack (U_{stack}) declared in Table 5 for each model.

$$I_j/I = 1 + \frac{U_{stack}}{NIR^*_{i\text{-}o}}\frac{j}{2}(j-N), \tag{46}$$

where I_j is the current drained by the j-th electrode in a stack with N cells; $I = 1$ A is the total current, and $R^* = 106.4\ \Omega$ is the resistance of the inlet (in) or outlet (o) manifold. I_j is lower than I due to the leakage current through the electrolyte manifold between electrodes.

In order to quantify the reactor performance, it results convenient to introduce the fraction (ψ) of current lost because of the leakage current as

$$\psi = \frac{(I-I_1)+(I-I_2)+\cdots+(I-I_n)}{NI} = \frac{NI - \sum_{j=1}^{N} I_j}{NI}. \tag{47}$$

Figure 8B shows that Model 1 presents a more even distribution than Model 2, which is a consequence of the low conductivity of the solid phase in the latter case that promotes an increase in the leakage current, high ψ value in Table 5. Likewise, the distribution of current is more uniform for the 3D structure (blue line), which can be explained by considering that the increase in the surface area admits lower values of both overpotentials and Ohmic drop than in 2D configurations to drain the same current. This comportment is characterized by a low ψ value in Table 5. Taking into account the dashed lines, the current fraction according to the electrical analog model (Equation 46) is always higher than the values for the other models. This behavior can be understood by considering that the change in polarization resistance along the electrode in the computational algorithms enlarges the axial current distribution, and it is also an additional term that increases the leakage current. Moreover, numerical procedures permit a more detailed description of the geometry near the manifolds,

TABLE 3 Comparison between the numerical simulation and experimental results from González Pérez and Bisang[49]

I (A)	c_{in} (ppm)	$Q \times 10^6$ ($m^3\ s^{-1}$)	$\kappa_s \times 10^{-5}$ ($S\ m^{-1}$)	κ_f ($S\ m^{-1}$)	$L_{c,exp}$ (mm)	$L_{c,th}$ (mm)	I^*/I_{exp} (%)	I^*/I_{th} (%)
2	1015	6.0	2.383	3.94	2.04	**2.06**	78.3	**74.8**
3	382	6.0	2.383	5.10	5.61	**3.67**	75.5	**74.1**
3	472	19.7	2.383	3.80	3.82	**3.38**	55.9	**54.3**

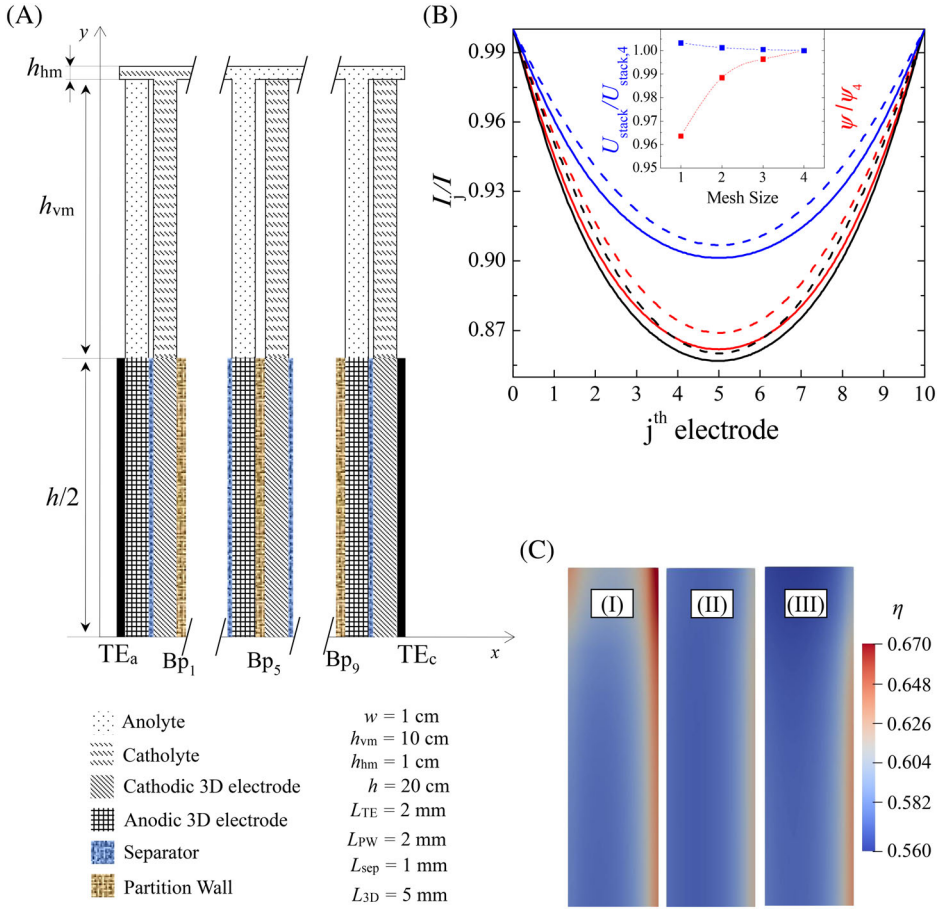

FIGURE 8 (A) Schematic representation of the upper half of a bipolar stack. (B) Current fraction as a function of electrode position in the cell stack using the physicochemical and kinetic parameters depicted in Table 4. Full red line: Model 1 and also in accordance with Colli and Girault,[29] Full black line: Model 2 and also from Colli and Bisang.[30] Full blue line: Model 3. Dashed lines: analytical results according to Burnett and Danly[20] (Equation 46) using $R^*_{in\text{-}o} = 106.4\ \Omega$. $I = 1$ A. Inset: mesh-independence study for Model 3 as a function of the mesh size given in Table 6. Blue symbols: $U_{stack}/U_{stack,4}$. Red symbols: $/_4$. (C) Anodic overpotential distribution according to Model 3. Part (I): three-dimensional terminal anode. Part (II): anodic part of the fifth bipolar electrode (Bp_5). Part (III): anodic part of the last bipolar electrode (Bp_9)

TABLE 4 Physicochemical and kinetic parameters used to model the bipolar stack

Model	1	2	3
κ_{TE} (S m^{-1})		1×10^7	
κ_{PW} (S m^{-1})	1×10^7	20	1000
$\kappa_{s\ 3D}$ (S m^{-1})	–	–	58
$\kappa_{f\ 3D}$ (S m^{-1})	–	–	19.6
κ_f (S m^{-1})		25	
κ_{sep} (S m^{-1})		10	
j_0 (A m^{-2})		1	
$b_{a\text{-}c}$ (V)		0.05	
A_s (m^{-1})	–	–	1000

TABLE 5 Model's results of the bipolar stack

Model	1	2	3
I (A)		1	
U_{stack} (V)	11.298	12.06	8.037
Ψ (%)[a]	9.63	10.06	6.89
Ψ (%)[b]	8.76	9.35	6.23

[a]Present strategy.
[b]From Burnett and Danly,[20] $R^*_{in\text{-}o} = 106.4\ \Omega$.

TABLE 6 Mesh properties

Mesh size	(x,y,z)
1	(132,22,2)
2	(264,44,2)
3	(396,63,2)
4	(528,84,2)

influencing both current density distribution and leakage current. Table 5 also shows that ψ for the electrical analog model is always lower than the values for the other computational proposals; concluding that, as expected, the leakage current is underestimated when the description of the geometry and the change of polarization resistance along spatial coordinates are disregarded.

Model 3 cannot be compared with previous calculations as it was made with Models 1 and 2. In order to corroborate its validity, a mesh-independence study was performed according to the mesh sizes given in Table 6. Therefore, the inset in Figure 8B displays the ratios of U_{stack} (blue symbols) and (red symbols) against the corresponding values for the finest mesh. The inset demonstrates that in all cases the size of the mesh is adequate due to the irrelevant change of results when the mesh is refined.

Figure 8C shows the anodic overpotential distribution for Model 3. Part (I) depicts the overpotential in the terminal anode, Part (II) and Part (III) correspond to the anodic region of the fifth and ninth bipolar electrode (Bp_5-Bp_9), respectively. As expected, in all cases, the higher overpotentials take place near the separator, where the maximum value in the region is close to the port of the electrolyte manifold for the TE and in the central zone for the bipolar ones. This finding can be explained by considering the effect of the leakage current on the current distribution in bipolar electrochemical reactors.[21] Therefore, the region near the inlet or outlet of the electrolyte has a larger contribution to the leakage current than the central region of the terminal anode, and the inverse situation occurs for bipolar electrodes. This statement was corroborated by Darling et al.[60] for the case of redox flow batteries. Furthermore, an intensive anodic reaction is also observed for the terminal anode in the upper part next to the current feeder, which is caused by the Ohmic drop inside the 3D structure.[12] It should be noted that the 3D cathodic regions show a performance similar to that of the anodic ones reported in Figure 8C. Also, it must be emphasized that the overpotential distribution is strongly dependent on the kinetics of the electrochemical system, which can be easily changed in the present solver, and variations in concentrations or in the properties of the 3D structure can also be considered in a simple way.

5 | CONCLUSIONS

A solver for the analysis of multiphysics problems involving electrochemical systems made up of 3D activated or resistive electrodes under a monopolar or bipolar connection has been developed using OpenFOAM.

The model accounts for multiple equation sets for fluid flow, species concentration, mass-transfer, chemical reactions, and electric charge existing in different regions, that is, 3D-solid–fluid, to obtain potential and current density distributions, cell/stack potential differences and total or leakage currents. It considers multiple reactions at each electrode with different kinetic controls and properties variation along spatial coordinates.

The proposed solver, whose flowchart is depicted in Figure 2, together with a tutorial is given as an open-source code[57] for the reader to use or modify and to demonstrate its capabilities.

The tool for 3D electrodes is consistent as it works appropriately to predict the behavior in many situations in which analytical, numerical, or experimental data are available, such as current and potential distribution in planar, porous with varying electrolyte conductivity, cylindrical, bipolar, and stack of bipolar 3D electrodes. It even enlarges the information about the results obtained where the aforementioned analytical or numerical analyses have their limitations.

Finally, the model for 3D electrodes can be employed to optimize stack design, such as redox flow batteries and system operating conditions, helping the designer to scale-up situations.

ACKNOWLEDGMENTS

This work was supported by Agencia Nacional de Promoción Científica y Tecnológica (ANPCyT), Consejo Nacional de Investigaciones Científicas y Técnicas (CONICET) and Universidad Nacional del Litoral (UNL) of Argentina.

NOTATION

a	constant given in Equation (9)
A_s	specific surface area, m^{-1}
b	Tafel slope $= RT/\alpha F$, V
b	exponent given in Equation (9)
c	concentration, mol m^{-3} or ppm
d_e	characteristic length, m
D_k	diffusion coefficient of the k-th species, $m^2\ s^{-1}$
D_T	turbulent diffusion coefficient, $m^2\ s^{-1}$
E	electrode potential, given by Equation (40), V
E^i_{rev}	equilibrium potential of the i-th reaction, V
$E^{0,i}$	equilibrium potential of the i-th reaction under standard conditions, V
f	function defined in Equations (25) and (27)
F	Faraday constant $= 96{,}485$, C mol^{-1}
h	electrode height, m
I	current, A
I^*	shunt, leakage, parasitic or bypass current given by Equation (45), A
j	referred to the j-th bipolar electrode
j	current density, A m^{-2}
j_0	exchange current density, A m^{-2}
J	dimensionless reaction rate, Equation (32)
J_f	dimensionless electrolyte current density, Equation (36)
k_m	mass-transfer coefficient, m s^{-1}
L	electrode thickness, m
m	exponent given in Equation (7)
N	number of cells in the stack
n	coordinate normal to surface, m
p	density normalized pressure, $m^2\ s^{-2}$
Q	volumetric flow rate, $m^3\ s^{-1}$
r	radial coordinate or radius, m
R	universal gas constant $= 8.314$, J K^{-1} mol^{-1}
R^i_k	chemical reaction source term, given in Equations (6) and (31), mol s^{-1} m^{-3}
R^*	manifold resistance appearing in Equation (46), Ω
Re	Reynolds number
S	source term given in Equation (12), m s^{-2}
Sc	Schmidt number
T	temperature, °C or K
$\boldsymbol{u}$	fluid velocity, m s^{-1}
U	potential difference, V
U_{stack}	stack potential difference, V
V	electrode volume, m^3
VR	function defined in Equations (25) and (28)
VGR	function defined in Equations (25) and (26)
w	electrode width, m
x	axial coordinate, m
X	dimensionless thickness, x/L

y axial coordinate, m
z axial coordinate, m

GREEK CHARACTERS

α apparent charge transfer coefficient
γ_k activity coefficient of the k-th species, given in Equation (5)
δ dimensionless number given by Equation (34)
Δ distance between the cell center to the interface
ε void fraction
η overpotential, V
θ dimensionless number given by Equation (33)
κ effective electrical conductivity, S m^{-1}
κ^0 electrical conductivity, S m^{-1}
ν kinematic viscosity, m^2 s^{-1}
ν_e stoichiometric coefficient of the electron
ν_k stoichiometric coefficient of the k-th species
ν_T turbulent kinematic viscosity, m^2 s^{-1}
ξ dimensionless number given by Equation (37)
σ dimensionless constant given by Equation (33)
τ dimensionless number given by Equation (34)
ϕ potential, V
χ dimensionless electrolyte potential, Equation (39)
ψ fraction of leakage current given by Equation (47)
Ω dimensionless number given by Equation (44)

SUBSCRIPTS

a anodic
app applied
av average
c cathodic
CF current feeder
e outer
exp experimental
ECR electronic conducting regions
f fluid phase
hm horizontal manifold
i inner
in inlet
ICR ionic conducting regions
j j-th bipolar electrode
k k-th species
lim limiting
ME massive electrode
nr next region
pr present region
ref = i for the outer, = e for the inner counter electrode
s solid phase
T turbulent
th theoretical
vm vertical manifold
w wall
3D three-dimensional structure

SUPERSCRIPT

a anodic
c cathodic
center referred to cell or volume element center
face referred to cell or volume element face
i referred to the i-th reaction
old older iteration step
T transpose of a tensor

ABBREVIATIONS

BC boundary condition
Bp bipolar electrode
CE counter electrode
CF current feeder
FVM finite volume method
PW partition wall
sep separator
TE terminal electrode
WE working electrode

AUTHOR CONTRIBUTIONS

Alejandro Colli: Conceptualization; funding acquisition; investigation; methodology; software; validation; writing - original draft; writing-review & editing. **José Bisang:** Conceptualization; funding acquisition; investigation; methodology; project administration; supervision; writing - original draft; writing-review & editing.

DATA AVAILABILITY STATEMENT

The data that supports the findings of this study are available within the article.

ORCID

Alejandro N. Colli https://orcid.org/0000-0002-0983-1842
José M. Bisang https://orcid.org/0000-0001-9120-7418

REFERENCES

1. Pletcher D, Walsh FC. *Industrial Electrochemistry*. 2nd ed. London: Chapman and Hall; 1993.
2. Jüttner K, Galla U, Schmieder H. Electrochemical approaches to environmental problems in the process industry. *Electrochim Acta*. 2000; 45(15–16):2575-2594.
3. Ruotolo LAM, Gubulin JC. A mathematical model to predict the electrode potential profile inside a polyaniline-modified reticulate vitreous carbon electrode operating in the potentiostatic reduction of Cr(VI). *Chem Eng J*. 2011;171(3):1170-1177.
4. Bennion DN, Newman J. Electrochemical removal of copper ions from very dilute solutions. *J Appl Electrochem*. 1972;2(2):113-122.
5. Pilone D, Kelsall GH. Model of multiple metal electrodeposition in porous electrodes. *J Electrochem Soc*. 2006;153(5):D85-D90.
6. Alkire RC, Gould RM. An engineering model for electro-organic synthesis in continuous flow-through porous electrodes. *J Electrochem Soc*. 1980;127(3):605-612.
7. Sun C, Delnick FM, Baggetto L, Veith GM, Zawodzinski TA. Hydrogen evolution at the negative electrode of the all-vanadium redox flow batteries. *J Power Sources*. 2014;248:560-564.

8. Newman J, Thomas-Alyea KE. *Electrochemical Systems*. 3rd ed. Hoboken, New Jersey: Wiley-Interscience; 2004.
9. Newman JS, Tobias CW. Theoretical analysis of current distribution in porous electrodes. *J Electrochem Soc*. 1962;109(12):1183-1191.
10. Coeuret F. The fluidized bed electrode for the continuous recovery of metals. *J Appl Electrochem*. 1980;10(6):687-696.
11. Sun YP, Xu WL, Scott K. An efficient method for solving the model equations of a two dimensional packed bed electrode. *J Appl Electrochem*. 1995;25(8):755-763.
12. Kreysa G, Jüttner K, Bisang JM. Cylindrical three-dimensional electrodes under limiting current conditions. *J Appl Electrochem*. 1993;23(7):707-714.
13. Alkire RC, Ng PK. Two-dimensional current distribution within a packed-bed electrochemical flow reactor. *J Electrochem Soc*. 1974;121(1):95-103.
14. Fedkiw PS. Ohmic potential drop in flow-through and flow-by porous electrodes. *J Electrochem Soc*. 1981;128(4):831-838.
15. Risch T, Newman J. A theoretical comparison of flow-through and flow-by porous electrodes at the limiting current. *J Electrochem Soc*. 1984;131(11):2551-2556.
16. Kreysa G, Reynvaan C. Optimal design of packed bed cells for high conversion. *J Appl Electrochem*. 1982;12(2):241-251.
17. Bergmann H, Hertwig K, Nieber F. Experimental and theoretical studies on a new type of electrochemical reactor for waste-water treatment. *Chem Eng Process*. 1992;31(3):195-203.
18. Yin C, Gao Y, Guo S, Tang H. A coupled three dimensional model of vanadium redox flow battery for flow field designs. *Energy*. 2014;74:886-895.
19. Zhou G, Chen L-D, Seaba JP. Effects of property variation and ideal solution assumption on the calculation of the limiting current density condition of alkaline fuel cells. *J Power Sources*. 2011;196(11):4923-4933.
20. Burnett JC, Danly DE. Current bypass in electrochemical cell assemblies. *AIChe Symp Ser*. 1979;75:8-13.
21. Henquín ER, Bisang JM. Simplified model to predict the effect of the leakage current on primary and secondary current distributions in electrochemical reactors with a bipolar electrode. *J Appl Electrochem*. 2005;35(12):1183-1190.
22. Kaminski EA, Savinell RF. A technique for calculating shunt leakage and cell currents in bipolar stacks having divided or undivided cells. *J Electrochem Soc*. 1983;130(5):1103-1107.
23. Fink H, Remy M. Shunt currents in vanadium flow batteries: measurement, modelling and implications for efficiency. *J Power Sources*. 2015;284:547-553.
24. Xing F, Zhang H, Ma X. Shunt current loss of the vanadium redox flow battery. *J Power Sources*. 2011;196(24):10753-10757.
25. Wandschneider FT, Röhm S, Fischer P, Pinkwart K, Tübke J, Nirschl H. A multi-stack simulation of shunt currents in vanadium redox flow batteries. *J Power Sources*. 2014;261:64-74.
26. Comninellis C, Plattner E, Bolomey P. Estimation of current bypass in a bipolar electrode stack from current-potential curves. *J Appl Electrochem*. 1991;21(5):415-418.
27. Rousar I, Thonstad J. Calculation of bypass currents in molten salt bipolar cells. *J Appl Electrochem*. 1994;24(11):1124-1132.
28. Henquín ER, Bisang JM. Effect of leakage currents on the secondary current distribution in bipolar electrochemical reactors. *J Appl Electrochem*. 2008;38(9):1259-1267.
29. Colli AN, Girault HH. Compact and general strategy for solving current and potential distribution in electrochemical cells composed of massive monopolar and bipolar electrodes. *J Electrochem Soc*. 2017;164(11):E3465-E3472.
30. Colli AN, Bisang JM. Current and potential distribution in electrochemical reactors with activated or resistive electrodes. A multiregion and open source approach. *Electrochim Acta*. 2018;290:676-685.
31. Yin C, Guo S, Fang H, Liu J, Li Y, Tang H. Numerical and experimental studies of stack shunt current for vanadium redox flow battery. *Appl Energy*. 2015;151:237-248.
32. Fleischmann M, Oldfield JW. Fluidised bed electrodes: part I. Polarisation predicted by simplified models. *J Electroanal Chem Interf Electrochemistry*. 1971;29(2):211-230.
33. Wendt H, Kreysa G. *Electrochemical Engineering: Science and Technology in Chemical and Other Industries*. Berlin, Germany: Springer; 1999.
34. Pickett DJ. *Electrochemical Reactor Design*. 2nd ed. Amsterdam, Netherlands: Elsevier; 1979.
35. Bard AJ, Faulkner LR. *Electrochemical Methods: Fundamentals and Applications*. New York: Wiley; 2000.
36. Colli AN, Bisang JM. Comparison of the performance of flow-by three-dimensional cylindrical electrochemical reactors with inner or outer counter electrode under limiting current conditions. *Electrochim Acta*. 2015;154(0):468-475.
37. Kreysa G, Kuhn M. Modelling of gas evolving electrolysis cells. I. The gas voidage problem. *J Appl Electrochem*. 1985;15(4):517-526.
38. El-Anadouli BE, Ateya BG. Effects of gas bubbles on the current and potential profiles within porous flow-through electrodes. *J Appl Electrochem*. 1992;22(3):277-284.
39. Sun YP, Wu B, Qiu O, Xu W, Scott K. An approximate solution to the model of a sparged packed bed electrode reactor. *J Appl Electrochem*. 2002;32(11):1219-1227.
40. Bisang JM. Theoretical and experimental studies of current distribution in gas-evolving electrochemical reactors with parallel-plate electrodes. *J Appl Electrochem*. 1991;21(9):760-766.
41. Kusik C, Meissner H. Electrolyte activity coefficients in inorganic processing. *AIChe Symp Ser*. 1978;74:14-20.
42. Colli AN, Bisang JM. A CFD study with analytical and experimental validation of laminar and turbulent mass-transfer in electrochemical reactors. *J Electrochem Soc*. 2018;165(2):E81-E88.
43. Colli AN, Fornés JP, González Pérez O, Bisang JM. Evaluation of a modified hydrocyclone as electrochemical reactor for processing of two-phase (gas-liquid) systems. *Electrochim Acta*. 2019;309:219-227.
44. Colli AN, Bisang JM. Coupling k convection-diffusion and Laplace equations in an open-source CFD model for tertiary current distribution calculations. *J Electrochem Soc*. 2020;167(1):013513.
45. de Lemos MJS. *Turbulence in Porous Media: Modeling and Applications*. Amsterdam, Netherlands: Elsevier Science; 2012.
46. Domaingo A, Langmayr D, Somogyi B, Almbauer R. A semi-implicit treatment of porous media in steady-state CFD. *Transp Porous Media*. 2016;112(2):451-466.
47. Medina H, Beechook A, Saul J, Porter S, Aleksandrova S, Benjamin S. Open source computational fluid dynamics using OpenFOAM. Paper presented at: Light Aircraft Design: Methods and Tools, London; 2015.
48. González Pérez O, Bisang JM. Theoretical and experimental study of electrochemical reactors with three-dimensional bipolar electrodes. *J Appl Electrochem*. 2010;40(3):709-718.
49. González Pérez O, Bisang JM. Modelling of three-dimensional bipolar electrodes with irreversible reactions. *J Appl Electrochem*. 2011;41(5):609-616.
50. Newman JS, Tiedemann W. Porous-electrode theory with battery applications. *AIChE J*. 1975;21(1):25-41.
51. Diwakar VD, Subramanian VR. Effect of varying electrolyte conductivity on the electrochemical behavior of porous electrodes. *J Electrochem Soc*. 2005;152(5):A984-A988.
52. Zhou XL, Zhao TS, An L, Zeng YK, Wei L. Modeling of ion transport through a porous separator in vanadium redox flow batteries. *J Power Sources*. 2016;327:67-76.
53. Bisang JM. Theoretical and experimental studies of the effect of side reactions in copper deposition from dilute solutions on packed-bed electrodes. *J Appl Electrochem*. 1996;26(2):135-142.
54. Storck A, Enriquez-Granados MA, Roger M, Coeuret F. The behaviour of porous electrodes in a flow-by regime—I. theoretical study. *Electrochim Acta Theriol*. 1982;27(2):293-301.

55. Moukalled F, Mangani L, Darwish M. *The Finite Volume Method in Computational Fluid Dynamics: An Advanced Introduction with OpenFOAM® and Matlab*. Cham, Switzerland: Springer International Publishing; 2015.
56. Patankar SV. *Numerical Heat Transfer and Fluid Flow*. Boca Raton, FL: Taylor & Francis; 1980.
57. Colli AN. 3DSolidFluidMultiregionPotentialFoam, 2020, https://github.com/ancolli/3DSolidFluidMultiregionPotentialFoam.
58. openfoam, https://openfoam.org.
59. Guo Q, Cayetano M, Tsou Y-M, De Castro ES, White RE. Study of ionic conductivity profiles of the air cathode of a PEMFC by AC impedance spectroscopy. *J Electrochem Soc*. 2003;150(11):A1440.
60. Darling RM, Shiau H-S, Weber AZ, Perry ML. The relationship between shunt currents and edge corrosion in flow batteries. *J Electrochem Soc*. 2017;164(11):E3081-E3091.

How to cite this article: Colli AN, Bisang JM. A multi-region and open-source computational fluid dynamic tool for electrochemical systems with three-dimensional electrodes. *AIChE J*. 2021;67(11):e17371. https://doi.org/10.1002/aic.17371